Article

Li$_2$(BH$_4$)(NH$_2$) Nanoconfined in SBA-15 as Solid-State Electrolyte for Lithium Batteries

Qianyi Yang, Fuqiang Lu, Yulin Liu, Yijie Zhang, Xiujuan Wang, Yuepeng Pang * and Shiyou Zheng

School of Material Science and Engineering, University of Shanghai for Science and Technology, Shanghai 200093, China; 1826410107@st.usst.edu.cn (Q.Y.); 1826410208@st.usst.edu.cn (F.L.); 193742733@st.usst.edu.cn (Y.L.); 1826410131@st.usst.edu.cn (Y.Z.); 1826410104@st.usst.edu.cn (X.W.); syzheng@usst.edu.cn (S.Z.)
* Correspondence: pangyp@usst.edu.cn

Abstract: Solid electrolytes with high Li-ion conductivity and electrochemical stability are very important for developing high-performance all-solid-state batteries. In this work, Li$_2$(BH$_4$)(NH$_2$) is nanoconfined in the mesoporous silica molecule sieve (SBA-15) using a melting–infiltration approach. This electrolyte exhibits excellent Li-ion conduction properties, achieving a Li-ion conductivity of 5.0×10^{-3} S cm^{-1} at 55 °C, an electrochemical stability window of 0 to 3.2 V and a Li-ion transference number of 0.97. In addition, this electrolyte can enable the stable cycling of Li | Li$_2$(BH$_4$)(NH$_2$)@SBA-15 | TiS$_2$ cells, which exhibit a reversible specific capacity of 150 mAh g^{-1} with a Coulombic efficiency of 96% after 55 cycles.

Keywords: lithium borohydrides; lithium amides; nanoconfinement; solid electrolytes; all-solid-state batteries

1. Introduction

Enhancing the energy density and safety of rechargeable lithium batteries is extremely crucial for widespread applications, including electronic vehicles, integrated electronic devices, and smart grids [1–3]. Today, the current research hotspot of lithium batteries has been mainly centered on the exploration of advanced electrolytes with high ionic conductivity and electrochemical stability [4,5]. Nevertheless, although traditional organic liquid electrolytes exhibit excellent ionic conductivity, they inevitably suffer from inadequate electrochemical stabilities, dendritic Li growth, and serious safety hazards from battery combustion and explosion [6,7].

In view of these concerns, replacement of liquid electrolytes with mechanically rigid, nonflammable solid-state electrolytes (SSEs) will not only ensure safety during the lithium battery cycling but also significantly suppress dendritic Li formation [8–10]. Many families of SSEs with remarkable Li-ion conductivities have been proposed and investigated in the past few decades. Recently developed SSEs, including polymers (PEO-lithium salts [11–13]), oxides (perovskite-type [14,15], NASICON [16,17], LISICON [18,19], and garnet-type [20,21]), and thiophosphates (Li$_{10}$GeP$_2$S$_{12}$ [22] and Li$_2$S-P$_2$S$_5$ [23–25]), show considerably high Li-ion conductivities on the order of 10^{-7} to 10^{-3} S cm^{-1}. However, in spite of the high conductivity, most of these SSEs fail to fulfill the requirement of enough electrochemical stability with active electrode materials, thus hampering their further applications in all-solid-state lithium batteries (ASSLBs) [26–28].

Lithium borohydrides, members of the family of complex metal hydrides and well-known candidates for hydrogen storage [29–31], have drawn intense research interests and proved to be a new class of promising SSEs for ASSLBs because of their excellent Li-ion conduction properties [32,33]. As a representative material, LiBH$_4$, in the hexagonal phase (*P6$_3$mc*), exhibits high ionic conductivity (10^{-3} S cm^{-1}) at 120 °C, while its phase transformation to orthorhombic phase (*Pnma*) occurs below 110 °C, leading to a significant decrease in its Li-ion conductivity (<10^{-7} S cm^{-1} at room temperature (RT)) [34].

Improving the ionic conductivity of $LiBH_4$ at low temperature is important for its widespread application in ASSLBs. Matsuo et al. have reported that $Li_2(BH_4)(NH_2)$, formed by the ball milling of $LiBH_4$ and $LiNH_2$, showed an ionic conductivity four orders of magnitude higher than that of $LiBH_4$ at RT, which is attributed to the combination of $(BH_4)^-$ and $(NH_2)^-$ providing more occupation sites for the Li–ion [35]. Similar enhancements in ionic conductivity were realized via phase modifications [21,36–39]. Additionally, Blanchard et al. demonstrated that nanoconfinement of $LiBH_4$ in ordered mesoporous silica scaffolds (MCM-14) notably increases the Li-ion conductivity to 10^{-4} S cm^{-1} at 55 °C owing to the fast anion mobilities of $(BH_4)^-$ near the scaffold wall [40]. Furthermore, it is reported that the ionic conductivity of $LiBH_4$–$LiNH_2$/metal oxide nanocomposites could be improved by stabilization of a highly conductive phase inside the scaffold pores [41]. However, further in-depth investigation on applying these SSEs in ASSLBs is still highly essential.

In this work, we conducted research on confining highly ion-conductive $Li_2(BH_4)(NH_2)$ in nanopores of the mesoporous silica molecule sieve (SBA-15). The synergic effect generated by the combination of $(NH_2)^-$ substitution and SBA-15 nanoconfinement results in considerably enhanced ionic conductivity and electrochemical stability of $Li_2(BH_4)(NH_2)@SBA$-15. More importantly, the outstanding Li-ion conduction properties of $Li_2(BH_4)(NH_2)@SBA$-15 enable the stable cycling of Li | | TiS_2 ASSLBs.

2. Materials and Methods

2.1. Materials Synthesis

All preparations and manipulations of materials were performed in a glove box with a circulation purifier (Ar atmosphere, <0.1 ppm O_2 and H_2O). $LiBH_4$ (95%, Sigma-Aldrich, Shanghai, China) and $LiNH_2$ (99.95%, Sigma-Aldrich, Shanghai, China) were used as received without further purification. SBA-15 was prepared according to the method introduced in the literature [42] and dried under dynamic vacuum at 250 °C for 12 h prior to use. $LiBH_4$ and $LiNH_2$ in a molar ratio of 1:1 were ball-milled at 400 rpm for 12 h under an Ar atmosphere. The mixture was then heated at 5 °C min^{-1} to 120 °C and held under a 100-bar H_2 atmosphere for 12 h to obtain $Li_2(BH_4)(NH_2)$. $Li_2(BH_4)(NH_2)@SBA$-15 was synthesized by heating a mixture of SBA-15 and milled $Li_2(BH_4)(NH_2)$ with different weight ratios (60:40, 50:50, 30:70, 20:80) under 100-bar H_2 at 95 °C for 3 h. Afterwards, the sample was cooled and transferred to the Ar-filled glove box.

2.2. Structural Characterization

X-ray diffraction (XRD) measurements were conducted with homemade holders on a MiniFlex 600 (Rigaku Corporation, Tokyo, Japan) at a scan rate of 5° min^{-1}. Fourier-transform infrared spectroscopy (FTIR) was recorded by a Vector 22 (Bruker Corporation, Billerica, MA, USA) in transmission mode. Scanning electron microscopy (SEM) observations and energy dispersive X-ray spectroscopy (EDS) mapping were performed on a Nova SEM 230 (FEI, Hillsboro, OH, USA) equipped with an X-Max 80 (INCA, Abingdon, UK). The structural information of specific surface areas, pore volumes, and radii were analyzed on an ASAP2020 (Micromeritics Instrument Corporation, Norcross, GA, USA) using the Brunauer–Emmett–Teller (BET) and Barrett–Joyner–Halenda (BJH) methods.

2.3. Cell Assemblies and Electrochemical Measurements

All-solid-state cells were assembled using homemade Swagelok-type dies of 10 mm-diameter under 400 MPa pressure. The thickness of the electrolyte pellets was 3 mm for the Li-ion conduction measurement and 0.7 mm for other electrochemical measurements. For the Li | | TiS_2 cells, the anode was Li foil (99.5%) of 6 mm-diameter, and the cathode was a TiS_2-based composite (8 mg, 50 wt% TiS_2, 25 wt% $Li_2(BH_4)(NH_2)@SBA$-15, 25 wt% C) pressed into pellets of 8-mm diameter and less than 0.02 mm thickness.

Electrochemical impedance spectroscopy (EIS), direct current (DC) polarization, and cyclic voltammetry (CV) were conducted on an Interface 1000E (Gamry Instruments, Warminster, England). Galvanostatic charge/discharge (GCD) curves were recorded for

the Li||TiS$_2$ ASSLBs using a CT2001A battery tester (LAND, Wuhan, China) at different current densities. The conductivity (σ) was calculated from the EIS of blocking cells. A depressed semicircle and a linear tail were observed in each Nyquist plot, in which the intersection of the semicircle with the Z' axis corresponds to the resistance (R). The conductivity can be derived from the following equation:

$$\sigma = \frac{d}{AR},\qquad(1)$$

where d is the thickness, and A is the area of the electrolyte pellet. CV measurements of Li||Mo cells were carried out in the voltage range of -0.2–3.5 V with a rate of 0.5 mV s^{-1} at 55 °C, and that of the Li||TiS$_2$ cells were measured within 1.6–2.7 V with the same rate and temperature. The electronic transference number was estimated from the ratio of steady current to initial current in the 10 mV potential step curve of a Mo||Mo cell, and the Li-ion transference number was obtained from the same ratio of a Li||Li symmetric cell. The results were calculated from the following equation:

$$t_{e^-} = \frac{d \cdot I_{e^-}}{A \cdot \Delta V \cdot \sigma_T},\qquad(2)$$

$$t_{Li^+} = \frac{d \cdot I_{Li} + R_A}{A \cdot \Delta V \cdot R_B \cdot \sigma_T},\qquad(3)$$

where d and A are the thickness and area of electrolytes, respectively, σ_T is the overall conductivity, I_{e^-} and I_{Li^+} are the steady currents in the DC polarization tests, ΔV is the DC polarization potential, and R_B and R_A are the resistance before and after polarization, respectively.

The activation energy (E_a) was calculated from the Nernst–Einstein equation:

$$\ln(\sigma_T) = -\frac{E_a}{k_B T} + C,\qquad(4)$$

where k_B is the Boltzmann constant.

3. Results and Discussion

### 3.1. Preparation of Li$_2$(BH$_4$)(NH$_2$)@SBA-15

As illustrated in Figure 1, a 3-step preparation process is applied for Li$_2$(BH$_4$)(NH$_2$)@SBA-15 preparing. Firstly, LiBH$_4$ and LiNH$_2$ with a molar ratio of 1:1 was ball milled to form a mixture. Secondly, the mixture was then heated under 120 °C and 100 bar hydrogen for 12 h to generate Li$_2$(BH$_4$)(NH$_2$). Finally, Li$_2$(BH$_4$)(NH$_2$) is nanoconfined into SBA-15 by heating the mixtures of Li$_2$(BH$_4$)(NH$_2$) and SBA-15 at 95 °C and 100 bar hydrogen for 3 h.
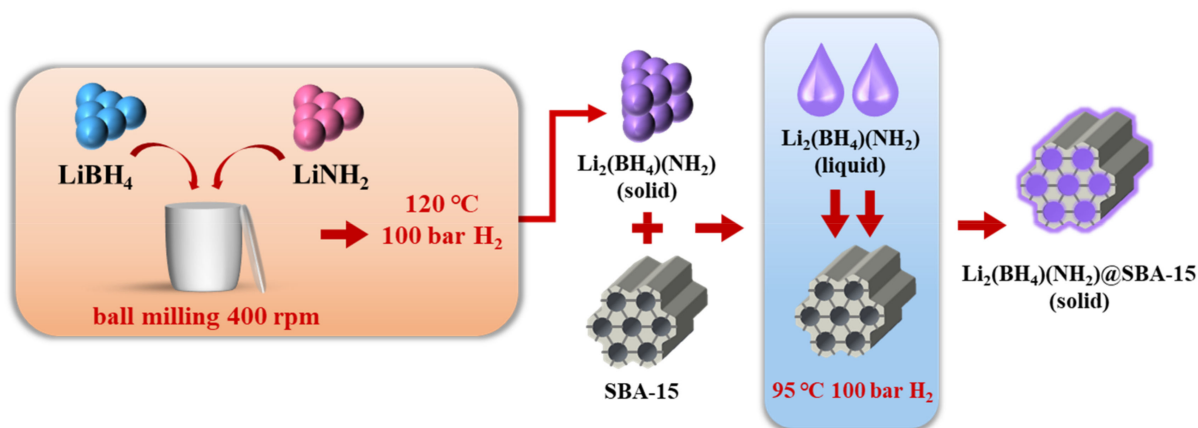
Figure 1. A schematic illustration of the $Li_2(BH_4)(NH_2)$@SBA-15 synthesis process.

3.2. Structures of $Li_2(BH_4)(NH_2)$@SBA-15

XRD was employed to clarify the phase composition of $Li_2(BH_4)(NH_2)$@SBA-15. As demonstrated in Figure 2a, the main peaks appearing in the $Li_2(BH_4)(NH_2)$ curve can be well-indexed to the pure phase at RT, suggesting a successful preparation. The characteristic peaks of $Li_2(BH_4)(NH_2)$ clearly remain in $Li_2(BH_4)(NH_2)$@SBA. These XRD patterns confirm that no phase transformation occurred in $Li_2(BH_4)(NH_2)$ after loading it into SBA-15.
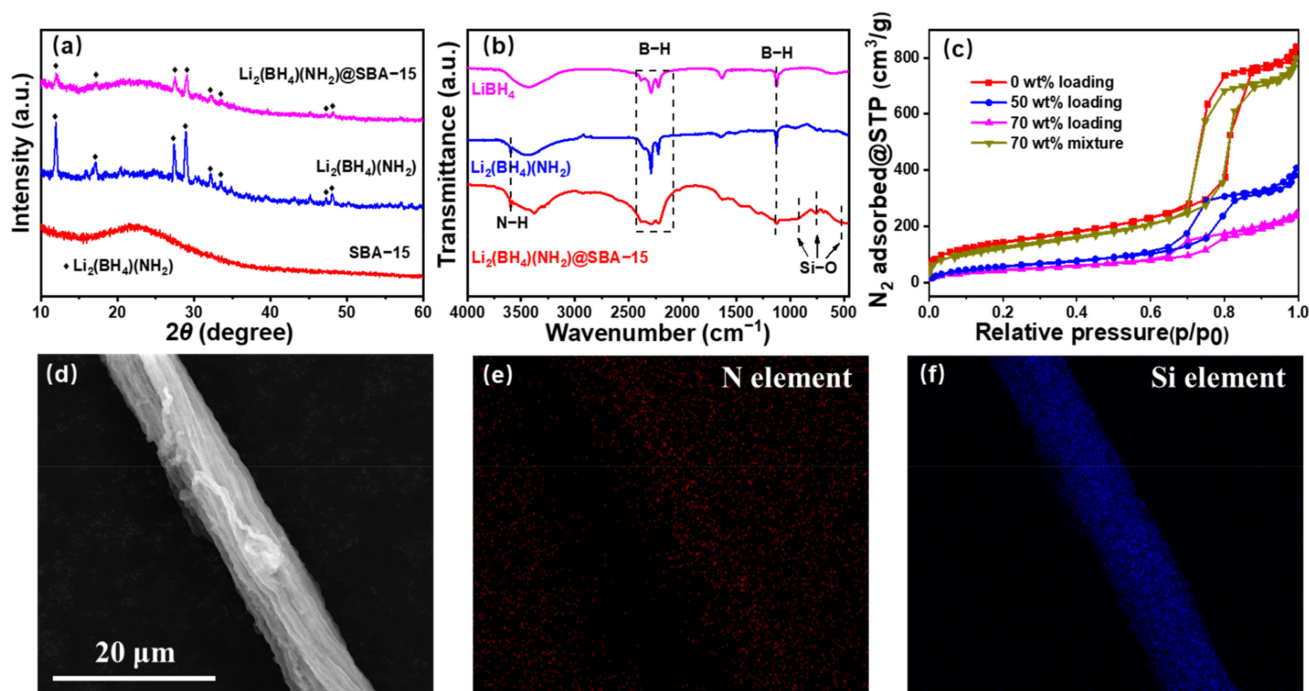
Figure 2. (**a**) X-ray diffraction (XRD) patterns of SBA-15, $Li_2(BH_4)(NH_2)$ and $Li_2(BH_4)(NH_2)$@SBA-15; (**b**) Fourier-transform infrared (FTIR) spectra of $Li_2(BH_4)(NH_2)$@SBA-15, $Li_2(BH_4)(NH_2)$ and $LiBH_4$; (**c**) N_2 absorption isotherms of SBA-15, $Li_2(BH_4)(NH_2)$/SBA-15, and $Li_2(BH_4)(NH_2)$@SBA-15; (**d**) scanning electron microscopy (SEM) images of $Li_2(BH_4)(NH_2)$@SBA-15; (**e,f**) energy dispersive X-ray spectroscopy (EDS) images of $Li_2(BH_4)(NH_2)$@SBA-15 illustrating the distribution of characteristic elements N and Si, respectively.

Considering that amorphous phases, which cannot be detected by XRD, may be generated from the decomposition of $Li_2(BH_4)(NH_2)$ [43], FTIR was used to further identify the phase composition of $Li_2(BH_4)(NH_2)$@SBA-15. As can be seen in the FTIR spectra

(Figure 2b), all peaks appearing in $Li_2(BH_4)(NH_2)$ belong to the stretching vibration of B–H and N–H. After loading $Li_2(BH_4)(NH_2)$ into SBA-15, the newly appearing peaks in $Li_2(BH_4)(NH_2)$@SBA-15 can be assigned to the Si–O bond, and no signal for decomposition byproducts of $Li_2(BH_4)(NH_2)$, such as Li–B–N compounds or B, is detected. These results are well in accordance with the previous discussion from the XRD patterns and indicate that the decomposition of $Li_2(BH_4)(NH_2)$ is totally suppressed by the presence of high-pressure hydrogen during the materials synthesis.

To further confirm the effective confinement of $Li_2(BH_4)(NH_2)$ into the SBA-15 mesopores by the melting–infiltration method, BET is applied to characterize the porosity parameters, as infiltration of $Li_2(BH_4)(NH_2)$ into SBA-15 may change the porosity of SBA-15. The porosities of SBA-15, 40 wt% $Li_2(BH_4)(NH_2)$@SBA-15, 70 wt% $Li_2(BH_4)(NH_2)$@SBA-15 and a 70 wt% $Li_2(BH_4)(NH_2)$/SBA-15 mixture were measured via nitrogen physisorption (normalized to 1g of SBA-15). Interpreted from the results in Figure 2c, the typical steep capillary condensation step and a hysteresis loop are observed in the pure SBA-15, agreeing well with the results for SBA-15 elsewhere [44]. Marked reductions in nitrogen absorption amounts were detected for the two melt-infiltrated $Li_2(BH_4)(NH_2)$@SBA-15 samples, while that of the $Li_2(BH_4)(NH_2)$/SBA-15 mixture generally remained unchanged. Combining these results with the pore parameter of SBA-15, we can conclude that the melted $Li_2(BH_4)(NH_2)$ was successfully infiltrated into the mesopores of SBA-15 via a capillary action, and 90% of the SBA-15 mesopores were filled with 70 wt%$Li_2(BH_4)(NH_2)$ (Table S1).

SEM and EDS mapping were employed for in-depth investigations of the morphology and elemental distribution of $Li_2(BH_4)(NH_2)$@SBA-15 after the melting–infiltration process. In Figure 2d, the typical morphology of the SBA-15 scaffolds is observed, indicating that it remained almost intact after being infiltrated (Figure 2d). The EDS mapping images (Figure 2e,f) show that the distribution patterns of characteristic elements (N and Si, respectively) match well with the shapes of SBA-15 fibers, suggesting that $Li_2(BH_4)(NH_2)$ was evenly distributed into the mesopores of the SBA-15 scaffolds.

The above results demonstrate that the pure $Li_2(BH_4)(NH_2)$ phase was formed by partially substituting $(BH_4)^-$ with $(NH_2)^-$ at 120 °C. The possible decomposition of $Li_2(BH_4)(NH_2)$ during the synthesis process was suppressed by the high-pressure hydrogen atmosphere. Furthermore, the melting–infiltration method at 95 °C successfully enables this new phase to be homogeneously nanoconfined into the mesoporous SBA-15.

3.3. Electrochemical Performances

The ionic conductivities of $LiBH_4$, $Li_2(BH_4)(NH_2)$, and $Li_2(BH_4)(NH_2)$@SBA-15 with different loading contents (40 wt%, 50 wt%, 70 wt%, and 80 wt%) were determined from the temperature-dependent EIS (Figure S1). The temperature range is set to be 35 to 55 °C, due to the thermostability of the electrolytes (Figure S2). As displayed in Figure 3a, $Li_2(BH_4)(NH_2)$ exhibits a remarkably enhanced conductivity of 1.6×10^{-5} S cm^{-1} at 35 °C, which is generally three orders of magnitude higher than that of the host hydride $LiBH_4$. This value even reaches 1×10^{-3} S cm^{-1} at 55 °C. As for $Li_2(BH_4)(NH_2)$@SBA-15, its conductivities in the same temperature range (from 35 °C to 55 °C) are further improved by the nanoconfinement, from 2.8×10^{-4} S cm^{-1} to 5.0×10^{-3} S cm^{-1}. These increased conductivities can be attributed to the synergetic effect of $(NH_2)^-$ substitution and SBA-15 nanoconfinement. Moreover, the conductivity of $Li_2(BH_4)(NH_2)$@SBA-15 varies with the different loading contents of $Li_2(BH_4)(NH_2)$, among which the maximum effective loading content (70 wt%) generates the most distinguished enhancement in conductivity (Figure S3). The E_a of $Li_2(BH_4)(NH_2)$@SBA-15 is calculated to be 0.49 eV, which is typical for superior ionic conductors (<0.5 eV) [45].
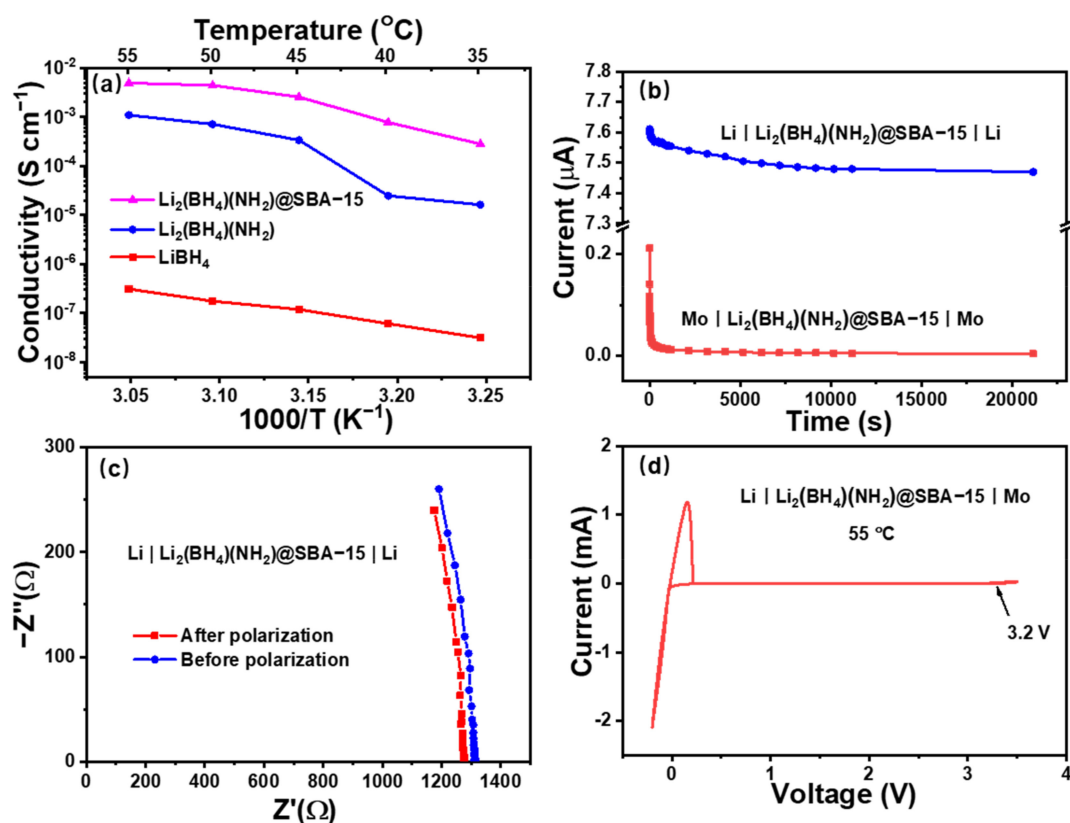
Figure 3. (**a**) Temperature-dependent conductivities of $LiBH_4$, $Li_2(BH_4)(NH_2)$ and $Li_2(BH_4)(NH_2)$@SBA-15; (**b,c**) electron and Li-ion transference numbers of $Li_2(BH_4)(NH_2)$@SBA-15, respectively; (**d**) cyclic voltammetry (CV) measurements of $Li_2(BH_4)(NH_2)$@SBA-15.

The transference numbers of $Li_2(BH_4)(NH_2)$@SBA-15 can be further characterized by DC polarization and EIS. Figure 3c presents the results of DC polarization tested on a Mo | $Li_2(BH_4)(NH_2)$@SBA-15 | Mo cell at 55 °C, showing that the steady current at 10 mV was extremely small, which corresponds to an electronic transference number very close to 0. Additionally, the Li-ion transference number of $Li_2(BH_4)(NH_2)$@SBA-15 was calculated to be 0.97, from the initial and steady currents, as well as the resistances recorded before and after polarization of Li | $Li_2(BH_4)(NH_2)$@SBA-15 | Li cells (Figure 3d). These results combined with the aforementioned ionic conductivities suggest that $Li_2(BH_4)(NH_2)$@SBA-15 possesses appreciable Li-ion conducting properties.

These results combined with the XRD patterns and FTIR spectra indicate the enhanced conduction properties can be well attributed to the successful incorporation of $Li_2(BH_4)(NH_2)$ into the mesopores of SBA-15. First, $Li_2(BH_4)(NH_2)$ itself has high Li-ion conductivity, which provides more occupation sites for mobile Li-ions than $LiBH_4$. Second, the SBA-15 nanoconfinement generate large $Li_2(BH_4)(NH_2)/SiO_2$ interface, which may result in a highly Li-ion conductive region due to the interface effect, as illustrated in literatures published elsewhere [46,47].

High ionic conductivity is one favorable requirement for an SSE. Besides this, the electrochemical stability and electrode compatibility of $Li_2(BH_4)(NH_2)$@SBA-15 also play essential roles in its application to ASSLBs. To test the electrochemical stability of $Li_2(BH_4)(NH_2)$@SBA-15, CV measurements were performed on Li | $Li_2(BH_4)(NH_2)$@SBA-15 | Mo cells at 55 °C (Figure 3b). In the −0.2 V to 3.5 V curve, redox peaks are only observed near 0 V and 3.2 V, which are related to the Li plating/stripping reaction on the Mo electrode and decomposition of $Li_2(BH_4)(NH_2)$, respectively. This result indicates that the apparent electrochemical stability window of $Li_2(BH_4)(NH_2)$@SBA is 0 to 3.2 V.

Considering the electrochemical window of $Li_2(BH_4)(NH_2)$@SBA-15 and the electrochemical compatibility of TiS_2 with the $LiBH_4$-based electrolytes [39,48], we employed

Li | | TiS$_2$ cells to evaluate the compatibilities of Li$_2$(BH$_4$)(NH$_2$)@SBA-15 with the electrode materials. In the CV measurements (Figure 4a) at 55 °C, the two adjacent peaks appearing at 2.2 and 1.8 V in anodic sweep correspond to the lithiation which can be described by the reaction TiS$_2$ + Li$^+$ + e$^-$ → LiTiS$_2$. Moreover, three oxidative peaks are observed in the cathodic sweep at 2.0, 2.4 and 2.7 V. The first two oxidative peaks can be interpreted by the delithiation reaction of LiTiS$_2$ (LiTiS$_2$ → TiS$_2$ + Li$^+$ + e$^-$), while the third one appearing at 2.7 V is due to the irreversible side-reaction which formed a solid electrolyte interface (SEI) film on the cathode side. In the subsequent cathodic sweeps, the peak intensities at 2.7 V decrease obviously, while integration areas and other peak positions remain almost unchanged, indicating that the side reaction was prevented by the SEI and the Li-ion insertion, and the extraction was relatively stable during cycling. Overall, the CV curves reflect that Li$_2$(BH$_4$)(NH$_2$)@SBA-15 is highly compatible with the Li and TiS$_2$ electrodes.
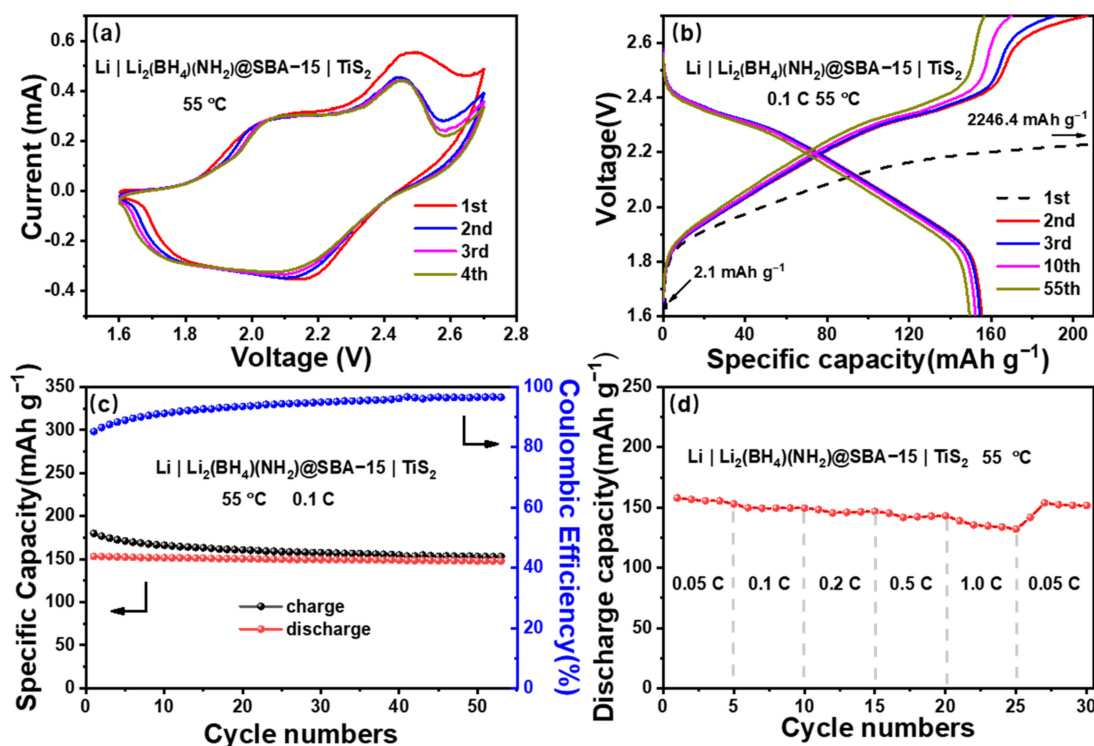
Figure 4. The electrochemical stabilities and cycling performances of Li | | TiS$_2$: (**a**) CV measurements within the potential range of 1.6–2.7 V; (**b**) charge/discharge profiles in the 1st, 2nd, 3rd, 10th, and 55th cycles; (**c**) cycling performances at 0.1 C and 55 °C; (**d**) rate capability behavior for 0.05 C–1 C.

The typical charge/discharge profiles and cycling performances of Li | | TiS$_2$ were profiled by GCD measurements at 0.1 C and 55 °C (Figure 4b,c). From the figures, the initial discharge capacity is relatively low, owing to the self-discharge reaction between TiS$_2$ and Li$_2$(BH$_4$)(NH$_2$)@SBA-15. The subsequent initial charging capacity is far exceeding the theoretical capacity of TiS$_2$ (239 mAh g^{-1}), which is similar to previous researches involving the same Li and TiS$_2$ electrode [49]. This phenomenon is attributed to the irreversible oxidative decomposition of Li$_2$(BH$_4$)(NH$_2$)@SBA-15 during the charging process.

Two plateaus at 2.3 and 1.9 V are present in the discharging curves in the overall cycling operation, and the discharging capacity is well retained at 150 mAh g^{-1} during the subsequent 55 cycles. In the second charging curve, three voltage plateaus are observed at 1.9, 2.3 and 2.6 V, with the total specific capacities of 207 mAh g^{-1}. Subsequently, the third voltage plateau gradually diminishes thereafter, which is in accordance with the CV curves. A stable charging capacity at 155 mAh g^{-1} was produced during the following 55 cycles. The Coulombic efficiency of the Li | | TiS$_2$ cell gradually increased after the formation of a stable SEI and was maintained at 96%.

Displayed in Figure 4d is the rate capability behavior of the Li||TiS$_2$ cells, determined by increasing the cycling charge/discharge rates every 5 cycles from 0.05 C to 1 C and then decreasing the rate to 0.05 C. The reversible discharge capacities measured at 0.05 C, 0.1 C, 0.2 C, 0.5 C, and 1 C are 155, 149, 146, 142, and 135 mAh g^{-1}, respectively. Significant decreases in capacities delivered at increasingly higher current densities are not observed. In addition, the capacity of the Li||TiS$_2$ cell was able to recover to 152 mAh g^{-1} at 0.05 C after cycling at high rates. These properties suggest that the (NH$_2$)$^-$ substitution and SBA-15 nanoconfinement are able to synergically improve the ionic conductivity of Li$_2$(BH$_4$)(NH$_2$)@SBA-15 as a promising SSE for ASSLBs.

4. Conclusions

In summary, we have demonstrated the successful preparation of Li$_2$(BH$_4$)(NH$_2$)@SBA-15 by (NH$_2$)$^-$ substitution and SBA-15 nanoconfinement (a comparison with relevant materials is show in Table 1). Li$_2$(BH$_4$)(NH$_2$)@SBA-15 with 70 wt% loading content exhibited the most significantly enhanced electric conductivity of 2.8×10^{-4} S cm^{-1} to 5.0×10^{-3} S cm^{-1} in the temperature range of 35–55 °C. The synergic effect of (NH$_2$)$^-$ substitution and SBA-15 nanoconfinement also provided an extremely low electronic transference number and a Li-ionic transference number of 0.97 at 55 °C, as well as an apparent electrochemical window of 0 to 3.2 V. Furthermore, overall electrochemical performances of Li$_2$(BH$_4$)(NH$_2$)@SBA-15 were investigated by application in Li||TiS$_2$ ASSLBs. The Li||TiS$_2$ cell delivered a reversible specific capacity of 150 mAh g^{-1} with a Coulombic efficiency of 96% after 55 cycles. The capacities were 155, 149, 146, 142, and 135 mAh g^{-1} at 0.05 C, 0.1 C, 0.2 C, 0.5 C, and 1 C rates, respectively. Moreover, the appearance of an additional plateau in the initial charging processes indicated a side reaction between Li$_2$(BH$_4$)(NH$_2$)@SBA-15 and cathode to form a protective SEI. Further investigations on the identification of this SEI will be carried out in our future works.

Table 1. Li-ion conduction properties of present LiBH$_4$-based materials and their present applications in all-solid-state lithium batteries (ASSLBs).

LiBH$_4$-Based Materials	$\sigma_{55°C}$ [1] (S cm^{-1})	E_a [2] (eV)	Electrochemical Window (V vs. Li/Li$^+$)	Applications in ASSLBs	Ref.
LiBH$_4$ ($P6_3mc$)	10^{-3} (120 °C)	0.53	5	Li||TiS$_2$	[34,48]
LiBH$_4$ ($Pnma$)	10^{-8}	0.69	5	-	[34]
LiBH$_4$@SBA-15	9×10^{-4}	0.43	3.5	Li||S	[40,50]
Li$_2$(BH$_4$)(NH$_2$)	9×10^{-4}	0.66	-	-	[32,35]
Li(NH$_3$)$_n$BH$_4$ ($0.5 \leq n \leq 1$)	10^{-3}–10^{-2} (40 °C)	-	4	-	[37]
LiBH$_4$–LiX (X = Cl, Br and I)	10^{-6}–10^{-4}	0.39–0.64	-	LiNbO$_3$-coated LiCoO$_2$/KB/80Li$_2$S 20P$_2$S$_5$||Li	[32,49]
LiBH$_4$−MgO composites	9×10^{-3}	0.29	2.2	Li||TiS$_2$	[39]
LiBH$_4$–LiNH$_2$/metal oxide nanocomposites	10^{-3}	0.86–0.90	-	-	[41]
Li$_4$(BH$_4$)$_3$I@SBA-15	8×10^{-3}	0.46	5	Li||Li$_4$Ti$_5$O$_{12}$, Li||S, Li||LiCoO$_2$	[44]
Li$_2$(BH$_4$)(NH$_2$)@SBA-15	5×10^{-3}	0.49	3.2	Li||TiS$_2$	-

[1] Li-ion conductivity at 55 °C; [2] Activation energy for Li-ion conduction.

Supplementary Materials: The following are available online at https://www.mdpi.com/article/10.3390/nano11040946/s1. Figure S1: A representative Nyquist plot of Li$_2$(BH$_4$)(NH$_2$)@SBA-15 derived from the electrochemical impedance spectroscopy (EIS) tests with an equivalent circuit, Figure S2. Thermogravimetric (TG) curve of Li$_2$(BH$_4$)(NH$_2$)@SBA-15, Figure S3: Conductivities of Li$_2$(BH$_4$)(NH$_2$)@SBA-15 with different loading contents of 40 wt%, 50 wt%, 70 wt% and 80 wt% at various temperatures, Table S1: Pore parameters of SBA-15, Li$_2$(BH$_4$)(NH$_2$)@SBA-15 samples and Li$_2$(BH$_4$)(NH$_2$)/SBA-15 mixtures.

References

1. Dunn, B.; Kamath, H.; Tarascon, J.-M. Electrical Energy Storage for the Grid: A Battery of Choices. *Science* **2011**, *334*, 928–935. [CrossRef]
2. Chu, S.; Cui, Y.; Liu, S.C.N. The path towards sustainable energy. *Nat. Mater.* **2017**, *16*, 16–22. [CrossRef] [PubMed]
3. Chu, S.; Majumdar, A. Opportunities and challenges for a sustainable energy future. *Nat. Cell Biol.* **2012**, *488*, 294–303. [CrossRef] [PubMed]
4. Cheng, X.-B.; Zhang, R.; Zhao, C.-Z.; Zhang, Q. Toward Safe Lithium Metal Anode in Rechargeable Batteries: A Review. *Chem. Rev.* **2017**, *117*, 10403–10473. [CrossRef] [PubMed]
5. Mauger, A.; Julien, C.M.; Paolella, A.; Armand, M.; Zaghib, K. Building Better Batteries in the Solid State: A Review. *Materials* **2019**, *12*, 3892. [CrossRef]
6. Wang, Y.; Zhong, W.-H. Development of Electrolytes towards Achieving Safe and High-Performance Energy-Storage Devices: A Review. *ChemElectroChem* **2014**, *2*, 22–36. [CrossRef]
7. Armand, M.; Tarascon, J.M. Building better batteries. *Nature* **2008**, *451*, 652–657. [CrossRef]
8. Tan, D.H.S.; Banerjee, A.; Chen, Z.; Meng, Y.S. From nanoscale interface characterization to sustainable energy storage using all-solid-state batteries. *Nat. Nanotechnol.* **2020**, *15*, 170–180. [CrossRef]
9. Manthiram, A.; Yu, X.; Wang, S. Lithium battery chemistries enabled by solid-state electrolytes. *Nat. Rev. Mater.* **2017**, *2*, 16103. [CrossRef]
10. Sun, Y.-K. Promising All-Solid-State Batteries for Future Electric Vehicles. *ACS Energy Lett.* **2020**, *5*, 3221–3223. [CrossRef]
11. Khurana, R.; Schaefer, J.L.; Archer, L.A.; Coates, G.W. Suppression of Lithium Dendrite Growth Using Cross-Linked Polyethylene/Poly(ethylene oxide) Electrolytes: A New Approach for Practical Lithium-Metal Polymer Batteries. *J. Am. Chem. Soc.* **2014**, *136*, 7395–7402. [CrossRef] [PubMed]
12. Choudhury, S.; Mangal, R.; Agrawal, A.; Archer, L.A. A highly reversible room-temperature lithium metal battery based on crosslinked hairy nanoparticles. *Nat. Commun.* **2015**, *6*, 10101. [CrossRef] [PubMed]
13. Martinez, U.; Babu, S.K.; Holby, E.F.; Zelenay, P. Durability challenges and perspective in the development of PGM-free electrocatalysts for the oxygen reduction reaction. *Curr. Opin. Electrochem.* **2018**, *9*, 224–232. [CrossRef]
14. Inaguma, Y.; Itoh, M. Influences of carrier concentration and site percolation on lithium ion conductivity in perovskite-type oxides. *Solid State Ion.* **1996**, *86-88*, 257–260. [CrossRef]
15. Amores, M.; El-Shinawi, H.; McClelland, I.; Yeandel, S.R.; Baker, P.J.; Smith, R.I.; Playford, H.Y.; Goddard, P.; Corr, S.A.; Cussen, E.J. $Li_{1.5}La_{1.5}MO_6$ (M = W^{6+}, Te^{6+}) as a new series of lithium-rich double perovskites for all-solid-state lithium-ion batteries. *Nat. Commun.* **2020**, *11*, 1–12. [CrossRef]
16. Kamaya, N.; Homma, K.; Yamakawa, Y.; Hirayama, M.; Kanno, R.; Yonemura, M.; Kamiyama, T.; Kato, Y.; Hama, S.; Kawamoto, K.; et al. A lithium superionic conductor. *Nat. Mater.* **2011**, *10*, 682–686. [CrossRef]
17. Tolganbek, N.; Yerkinbekova, Y.; Khairullin, A.; Bakenov, Z.; Kanamura, K.; Mentbayeva, A. Enhancing purity and ionic conductivity of NASICON-typed $Li_{1.3}Al_{0.3}Ti_{1.7}(PO_4)_3$ solid electrolyte. *Ceram. Int.* **2021**. [CrossRef]
18. Bruce, P.G.; West, A.R. The A-C Conductivity of Polycrystalline LISICON, $Li_{2+2x}Zn_{1-x}GeO_4$, and a Model for Intergranular Constriction Resistances. *J. Electrochem. Soc.* **1983**, *130*, 662–669. [CrossRef]
19. Reddy, M.V.; Julien, C.M.; Mauger, A.; Zaghib, K. Sulfide and Oxide Inorganic Solid Electrolytes for All-Solid-State Li Batteries: A Review. *Nanomaterials* **2020**, *10*, 1606. [CrossRef]
20. Kotobuki, M.; Kanamura, K.; Sato, Y.; Yoshida, T. Fabrication of all-solid-state lithium battery with lithium metal anode using Al_2O_3-added $Li_7La_3Zr_2O_{12}$ solid electrolyte. *Lancet* **2011**, *196*, 7750–7754. [CrossRef]
21. Gao, Y.; Sun, S.; Zhang, X.; Liu, Y.; Hu, J.; Huang, Z.; Gao, M.; Pan, H. Amorphous Dual-Layer Coating: Enabling High Li-Ion Conductivity of Non-Sintered Garnet-Type Solid Electrolyte. *Adv. Funct. Mater.* **2021**, 2009692. [CrossRef]
22. Mo, Y.; Ong, S.P.; Ceder, G. First Principles Study of the $Li_{10}GeP_2S_{12}$ Lithium Super Ionic Conductor Material. *Chem. Mater.* **2012**, *24*, 15–17. [CrossRef]
23. Hayashi, A.; Hama, S.; Minami, T.; Tatsumisago, M. Formation of superionic crystals from mechanically milled $Li_2S–P_2S_5$ glasses. *Electrochem. Commun.* **2003**, *5*, 111–114. [CrossRef]

24. Muramatsu, H.; Hayashi, A.; Ohtomo, T.; Hama, S.; Tatsumisago, M. Structural change of Li$_2$S–P$_2$S$_5$ sulfide solid electrolytes in the atmosphere. *Solid State Ion.* **2011**, *182*, 116–119. [CrossRef]

25. Kato, A.; Yamamoto, M.; Sakuda, A.; Hayashi, A.; Tatsumisago, M. Mechanical Properties of Li$_2$S–P$_2$S$_5$ Glasses with Lithium Halides and Application in All-Solid-State Batteries. *ACS Appl. Energy Mater.* **2018**, *1*, 1002–1007. [CrossRef]

26. Xu, K. Nonaqueous Liquid Electrolytes for Lithium-Based Rechargeable Batteries. *Chem. Rev.* **2004**, *104*, 4303–4418. [CrossRef]

27. Wan, J.; Xie, J.; Mackanic, D.; Burke, W.; Bao, Z.; Cui, Y. Status, promises, and challenges of nanocomposite solid-state electrolytes for safe and high performance lithium batteries. *Mater. Today Nano* **2018**, *4*, 1–16. [CrossRef]

28. Lim, H.-D.; Park, J.-H.; Shin, H.-J.; Jeong, J.; Kim, J.T.; Nam, K.-W.; Jung, H.-G.; Chung, K.Y. A review of challenges and issues concerning interfaces for all-solid-state batteries. *Energy Storage Mater.* **2019**, *25*, 224–250. [CrossRef]

29. Wang, Y.; Wan, C.; Meng, X.; Ju, X. Improvement of the LiBH$_4$ hydrogen desorption by confinement in modified carbon nanotubes. *J. Alloys Compd.* **2015**, *645*, S112–S116. [CrossRef]

30. Chen, K.; Ouyang, L.; Zhong, H.; Liu, J.; Wang, H.; Shao, H.; Zhang, Y.; Zhu, M. Converting H$^+$ from coordinated water into H$^-$ enables super facile synthesis of LiBH$_4$. *Green Chem.* **2019**, *21*, 4380–4387. [CrossRef]

31. Pang, Y.; Liu, Y.; Gao, M.; Ouyang, L.; Liu, J.; Wang, H.; Zhu, M.; Pan, H. A mechanical-force-driven physical vapour deposition approach to fabricating complex hydride nanostructures. *Nat. Commun.* **2014**, *5*, 3519. [CrossRef] [PubMed]

32. Matsuo, M.; Orimo, S.-I. Lithium Fast-Ionic Conduction in Complex Hydrides: Review and Prospects. *Adv. Energy Mater.* **2011**, *1*, 161–172. [CrossRef]

33. Campanella, D.; Belanger, D.; Paolella, A. Beyond garnets, phosphates and phosphosulfides solid electrolytes: New ceramic perspectives for all solid lithium metal batteries. *J. Power Sources* **2021**, *482*, 228949. [CrossRef]

34. Matsuo, M.; Nakamori, Y.; Orimo, S.-I.; Maekawa, H.; Takamura, H. Lithium superionic conduction in lithium borohydride accompanied by structural transition. *Appl. Phys. Lett.* **2007**, *91*, 224103. [CrossRef]

35. Motoaki, M. Complex hydrides with (BH$_4$)$^-$ and (NH$_2$)$^-$ anions as new lithium fast-ion conductors. *J. Am. Chem. Soc.* **2009**, *131*, 16389–16391.

36. Yan, Y.; Kühnel, R.-S.; Remhof, A.; Duchêne, L.; Reyes, E.C.; Rentsch, D.; Łodziana, Z.; Battaglia, C. A Lithium Amide-Borohydride Solid-State Electrolyte with Lithium-Ion Conductivities Comparable to Liquid Electrolytes. *Adv. Energy Mater.* **2017**, *7*, 7. [CrossRef]

37. Zhang, T.; Wang, Y.; Song, T.; Miyaoka, H.; Shinzato, K.; Miyaoka, H.; Ichikawa, T.; Shi, S.; Zhang, X.; Isobe, S.; et al. Ammonia, a Switch for Controlling High Ionic Conductivity in Lithium Borohydride Ammoniates. *Joule* **2018**, *2*, 1522–1533. [CrossRef]

38. Zhu, M.; Pang, Y.; Lu, F.; Shi, X.; Yang, J.; Zheng, S. In Situ Formed Li–B–H Complex with High Li-Ion Conductivity as a Potential Solid Electrolyte for Li Batteries. *ACS Appl. Mater. Interfaces* **2019**, *11*, 14136–14141. [CrossRef]

39. Gulino, V.; Brighi, M.; Murgia, F.; Ngene, P.; de Jongh, P.; Černý, R.; Baricco, M. Room-Temperature Solid-State Lithium-Ion Battery Using a LiBH$_4$–MgO Composite Electrolyte. *ACS Appl. Energy Mater.* **2021**, *4*, 1228–1236. [CrossRef]

40. Blanchard, D.; Nale, A.; Sveinbjörnsson, D.; Eggenhuisen, T.M.; Verkuijlen, M.H.W.; Suwarno; Vegge, T.; Kentgens, A.P.M.; de Jongh, P.E. Nanoconfined LiBH$_4$ as a Fast Lithium Ion Conductor. *Adv. Funct. Mater.* **2015**, *25*, 184–192. [CrossRef]

41. De Kort, L.M.; Harmel, J.; de Jongh, P.E.; Ngene, P. The effect of nanoscaffold porosity and surface chemistry on the Li-ion conductivity of LiBH$_4$-LiNH$_2$/metal oxide nanocomposites. *J. Mater. Chem. A* **2020**, *8*, 20687–20697. [CrossRef]

42. Zhao, D.; Feng, J.; Huo, Q.; Melosh, N.; Fredrickson, G.H.; Chmelka, B.F.; Stucky, G.D. Triblock Copolymer Syntheses of Mesoporous Silica with Periodic 50 to 300 Angstrom Pores. *Science* **1998**, *279*, 548–552. [CrossRef] [PubMed]

43. Orimo, S.; Nakamori, Y.; Kitahara, G.; Miwa, K.; Ohba, N.; Towata, S.; Züttel, A. Dehydriding and rehydriding reactions of LiBH4. *J. Alloys Compd.* **2005**, *404*, 427–430. [CrossRef]

44. Lu, F.; Pang, Y.; Zhu, M.; Han, F.; Yang, J.; Fang, F.; Sun, D.; Zheng, S.; Wang, C. A High-Performance Li–B–H Electrolyte for All-Solid-State Li Batteries. *Adv. Funct. Mater.* **2019**, *29*, 1809219. [CrossRef]

45. He, X.; Zhu, Y.; Mo, Y. Origin of fast ion diffusion in super-ionic conductors. *Nat. Commun.* **2017**, *8*, 15893. [CrossRef]

46. Choi, Y.S.; Lee, Y.-S.; Oh, K.H.; Cho, Y.W. Interface-enhanced Li ion conduction in a LiBH$_4$–SiO$_2$ solid electrolyte. *Phys. Chem. Chem. Phys.* **2016**, *18*, 22540–22547. [CrossRef] [PubMed]

47. Lefevr, J.; Cervini, L.; Griffin, J.M.; Blanchard, D. Lithium Conductivity and Ions Dynamics in LiBH$_4$/SiO$_2$ Solid Electrolytes Studied by Solid-State NMR and Quasi-Elastic Neutron Scattering and Applied in Lithium–Sulfur Batteries. *J. Phys. Chem. C* **2018**, *122*, 15264–15275. [CrossRef]

48. Unemoto, A.; Ikeshoji, T.; Yasaku, S.; Matsuo, M.; Stavila, V.; Udovic, T.J.; Orimo, S.-I. Stable Interface Formation between TiS$_2$ and LiBH$_4$ in Bulk-Type All-Solid-State Lithium Batteries. *Chem. Mater.* **2015**, *27*, 5407–5416. [CrossRef]

49. Unemoto, A.; Nogami, G.; Tazawa, M.; Taniguchi, M.; Orimo, S.-I. Development of 4V-Class Bulk-Type All-Solid-State Lithium Rechargeable Batteries by a Combined Use of Complex Hydride and Sulfide Electrolytes for Room Temperature Operation. *Mater. Trans.* **2017**, *58*, 1063–1068. [CrossRef]

50. Das, S.; Ngene, P.; Norby, P.; Vegge, T.; De Jongh, P.E.; Blanchard, D. All-Solid-State Lithium-Sulfur Battery Based on a Nanoconfined LiBH$_4$ Electrolyte. *J. Electrochem. Soc.* **2016**, *163*, A2029–A2034. [CrossRef]